0254-6124/2022/42(4)-0519-17 *Chin. J. Space Sci.* 空间科学学报

CHEN Yuesong, TANG Yuhua, FAN Yu, YAN Jun, WANG Chi, ZOU Yongliao. Overview of the Latest Scientific Achievements of Chang'E-4 Mission of China's Lunar Exploration Project. *Chinese Journal of Space Science*, 2022, **42**(4): 519–535. DOI:10.11728/cjss2022.04.yg30

Overview of the Latest Scientific Achievements of Chang'E-4 Mission of China's Lunar Exploration Project*

CHEN Yuesong[1] TANG Yuhua[2] FAN Yu[1] YAN Jun[3]
WANG Chi[1,4] ZOU Yongliao[1,4]

1(*National Space Science Center*, *Chinese Academy of Sciences*, *Beijing* 100190)

2(*Lunar Exploration and Space Engineering Center*, *Beijing* 100190)

3(*National Astronomical Observatories*, *Chinese Academy of Sciences*, *Beijing* 100101)

4(*State Key Laboratory of Space Weather*, *National Space Science Center*, *Chinese Academy of Sciences*, *Beijing* 100190)

Abstract On 3 January 2019, the Chang'E-4 probe successfully landed in the Von Kármán crater in the South Pole-Aitken Basin on the far side of the Moon. On 4 January, the Yutu-2 rover was successfully separated from the lander and the scientific payloads were powered on to conduct scientific exploration. It was the first time that man-made probe achieved soft landing and roving on the far side of the Moon. Based on the data obtained by scientific payloads on the Chang'E-4, the research team obtained geological information such as landing area topography, structure and composition; demonstrated the existence of deep materials—mainly olivine and low-calcium pyroxene in the South Pole-Aitken Basin; achieved high-precision imaging of the layered structure of lunar subsurface in the roving area; discovered carbonaceous spheroidal meteorite residues and impact glass; preliminarily revealed the geological evolutionary history of the South Pole-Aitken Basin; for the first time, obtained information of the radiation dose of energetic particles at the lunar surface and the structure of the lunar neutral atomic energy spectrum; discovered the lunar mini-magnetosphere and contributed new knowledge of the radiation hazards at the lunar surface. This article summarizes the latest scientific achievement from the Chang'E-4 mission over the past three years.

Key words Chang'E-4, Scientific objectives, Scientific payloads, Scientific achievement

Classified index V47, P35

1 Chang'E-4 Mission Overview

The Chang'E-4 mission consists of three parts: the lander, Yutu-2 rover and Queqiao relay satellite. On 3 January 2019, Chang'E-4 probe successfully landed in the Von Kármán crater in the South Pole-Aitken Basin on the far side of the Moon. The exact landing position is 177.5991°E, 45.4446°S, and the elevation is about –5935 m[1] .

On 4 January, the Yutu-2 rover was successfully separated from the lander and rolled onto the lunar surface. The scientific payloads on board worked normally and the data were effectively transmitted down. Until May 2022, Chang'E-4 has worked on the lunar surface

---

* Supported by National Key Research and Development Program of China (2020YFE0202100)

Received July 5, 2022

E-mail: Fanyu@nssc.ac.cn

for 42 months and the rover has walked 1180 m (Fig.1)[2]. It became the longest working probe on the surface of the Moon.

Chang'E-4 has been in orbit for more than 3 years, scientific research achievements have been continuously produced, and summaries have been made in different periods or on different topics[3–5].

1.1 Scientific Objectives of Chang'E-4 Mission

There were four scientific objectives for Chang'E-4 mission: (i) low-frequency radio astronomical study on the lunar surface; (ii) shallow structure investigation at the lunar far side of roving area; (iii) the topographic and the mineralogical composition investigation for the lunar far side of roving area; (iv) neutrons radiation dose and neutral atoms study on lunar environment[6].

1.2 Scientific Payloads on Chang'E-4 Mission

To achieve the scientific objectives, there were nine scientific payloads equipped on the Chang'E-4, four of which were mounted on the lander.

(1) Landing Camera (LCAM). It turned on during the decent phase while landing on the Moon and obtained the lunar feature map and topographic map of the landing area at each altitude from 2 km to 4 m.

(2) Terrain Camera (TCAM). It was installed on the top of stand on the lander and obtained the optical image of the landing site. The imaging distance was 5 m to ∞.

(3) Low Frequency Spectrometer (LFS). It detected solar low-frequency radio features at 0.1 –80 MHz during the lunar day.

(4) Lunar Lander Neutron & Dosimetry (LND). It measured energetic particle radiation dose at the lunar surface, particles in the Earth's radiation belt, and secondary particles caused by galactic cosmic ray interactions with the lunar surface.

There were four scientific payloads mounted on the Yutu-2 rover.

(1) Panoramic Camera (PCAM). It was installed on the top of the mast above the rover and the imaging distance was 3 m to ∞. As the rover moved and the mast rotated, it could acquire 3D optical images of the lunar surface in the survey area.

(2) Lunar Penetrating Radar (LPR). It had high-frequency channel and low-frequency channel. While the rover was moving, it could detect the deep surface structure and the internal structure and thickness of the lunar soil along the rover's roving route.

(3) Visible and Near-Infrared Imaging Spectrometer (VNIS). It could obtain the spectrum of detection target at 450–2400 nm full band and the hyperspectral image data at the band range of 450–950 nm.

(4) Advanced Small Analyzer for Neutrals (ASAN). It could measure neutral atoms produced by

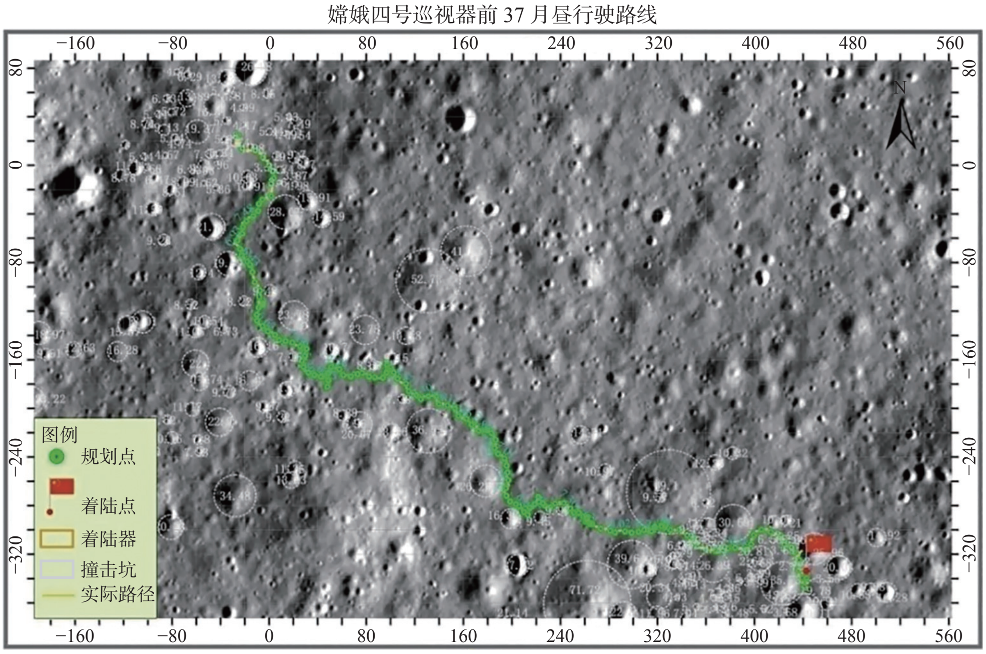

Fig. 1 Route map of the Yutu-2 rover

the interaction of the solar wind with the lunar surface, including the lunar soil material sputtered by the solar wind and the solar wind material scattered by the lunar surface.

The Netherlands-China Low Frequency Explorer Instrument (NCLE) on the communication relay satellite. It could acquire the sky background radio survey images at low-frequency bands for monitoring studies of planetary radio emission changes.

1.3 Operation of Scientific Payloads

Landing Camera. It was turned on during the decent phase and took pictures of the landing site. It just turned on one time and lasted for 9 min. After a successful soft landing on the Moon, the landing camera completed its exploration mission.

Terrain Camera. It worked on the first lunar day after landing and turned on 46 times. It completed imaging of low-frequency radio spectrometer antenna unlocking process, dynamic photographing movement at X-point and *in-situ* turning of the Rover, circling shooting with –60° to +45° pitch angle and taking pictures of the rover. While the lander entered the first lunar night, the terrain camera completed its exploration mission.

Panoramic Camera. It took pictures of the lander during the first lunar day and completed up-down circling shooting by color imaging during the second lunar day. It was turned on to take pictures when the rover drove to the detection point and it can be planned to take multiple sets of panchromatic or color images at fixed points when objects of interest occur.

LPR. It synchronously works while the rover is moving every lunar day.

VNIS. Imaging or calibration can be taken when the solar altitude angle is high around the lunar noon or objects of interest occur. It detects the tarcting rut of the rover and lunar soil, rocks and impact crater along the way.

ASAN. It starts to work when the solar altitude angle is high around the lunar noon or objects of interest occur. Detection modes include high voltage mode and ion mode.

LFS. It started to work at lunar noon to detect low-frequency signals from space.

LND. It chooses the opportunity to start working when the probe awakes in the lunar day. It can work during the whole lunar day.

2 Scientific Achievement of Chang'E-4

2.1 Topography of the Landing and Roving Area

2.1.1 Topography and Impact Crater Features

The major impact craters in the Von Kármán region include the Von Kármán M impact crater, the Von Kármán impact crater, the Leibnitz impact crater, the Finsen impact crater, the Alder impact crater, and the Von Kármán L and L' impact craters. The Von Kármán impact crater is located within a magnesite ring unit in the northwestern South Pole-Aitken Basin, and was flooded by one or more lunar mare basalt, after which ejecta from numerous impact craters in the surrounding area was ejected into its interior. The crater floor was modified by geologic processes such as impact ejecta, volcanism, and tectonic movement. A 5 cm resolution DEM covering 380 m×390 m was produced by panoramic stereoscopic images, revealing that the overall topography of the Von Kármán impact crater in the landing area is high in the northeast and low in the southwest, with wavy undulations in the southeast to northwest directions (Fig.2)[7]. At the 100 m baseline, the overall bottom of the Von Kármán impact crater is very flat, with a local slope of about 10°; at the 10 m baseline, the two-way slope near the landing site varies considerably, and the maximum slope in and around some impact craters can be greater than 20°; at the meter and tens of meters baselines, the two-way slope of the landing area is similar to that of the lunar mare (2.0°–3.4°)[8–10].

The basalt plain is covered with a large number of secondary craters formed by younger impact craters. Among them, the secondary crater formed by the Finsen impact crater from the east side of the Von Kármán impact crater has the most prominent influence on the topography of the landing site and the Yutu-2 roving route, and it is an important part of controlling the regional geomorphology. The secondary crater of the Finsen impact crater is significantly degraded and appears as a discrete linear depression and bulge in the topographic landscape. Using LROC NAC orthophotography, panoramic camera images, and 1 cm resolution DEMs, 4333 impact craters of 100 m or larger were extracted within the entire landing area (2.4°×1°, 51 km×30 km), 11787 impact craters were extracted in the area

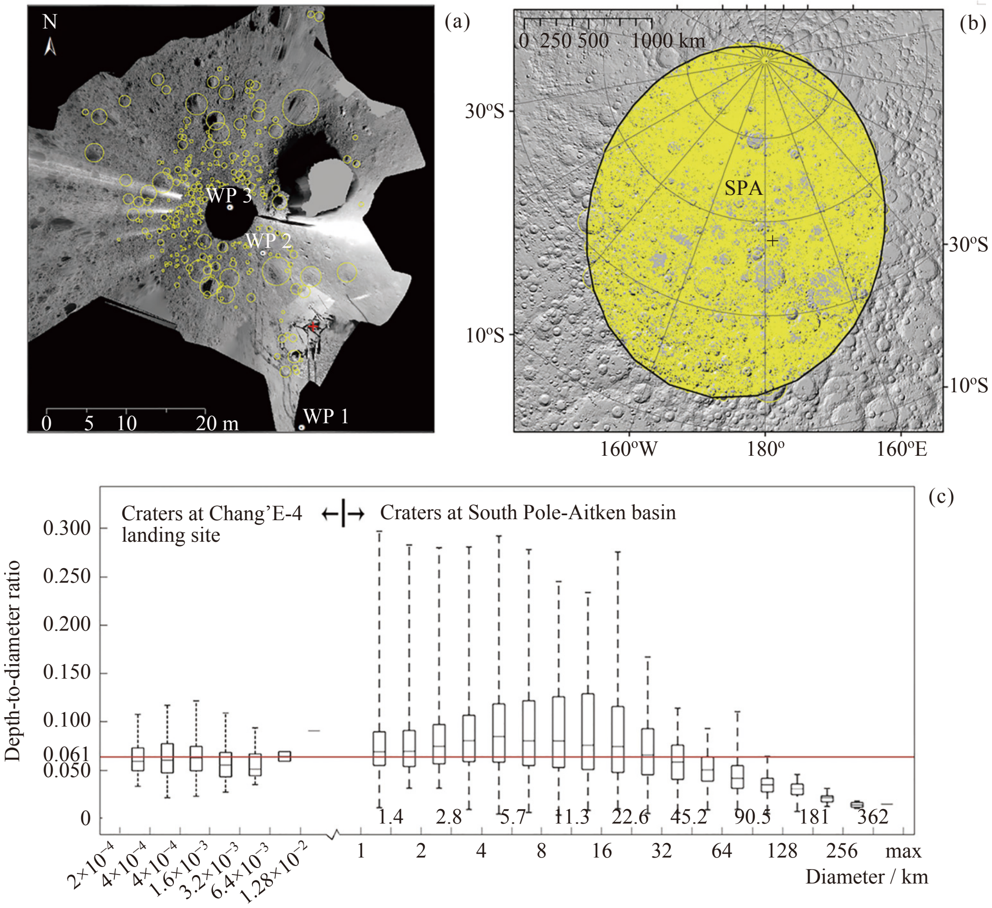

Fig. 2　Comparison of crater depth-to-diameter ratios between (a) small craters (>0.1 m) at Chang'E-4 landing site; and (b) large craters (>1 km) in the SPA basin; (c) box-and-whisker plot of crater depth-to-diameter ratios

of 3.2 km×3.0 km from the landing site, 738 impact craters of meter to sub-meter scale were extracted within 60 m from the camera, and 1023 impact craters of diameter larger than 10 cm were identified along the Yutu-2 roving route. Within 60 m, 738 impact craters of meter to sub-meter scale were extracted, 1023 impact craters with diameters larger than 10 cm were identified within 50 m×50 m of the landing site, and some fresh impact craters with diameters ranging from < 1 m to 3 m were scattered along the Yutu-2 roving route. The relationship between depth and diameter of impact craters has a good consistency, but the distribution of depth-diameter ratios is scattered, and the depth-diameter ratios of small impact craters at 10 cm scale are significantly smaller than those of kilometer-scale impact craters, indicating the inclusion of impact craters at different degradation stages and indicating the unique process of small impact crater formation in mature lunar soils[7, 11–14].

2.1.2　Characteristics of the Impact Ejecta

The thickness of the ejecta covered by the landing area is about 60–70 m, with the uppermost NE-SW distributed linear ejecta from Finsen Crater superimposed on the SE-NW ejecta from Adler Crater, and the thickness of ejecta from Finsen and Adler Craters at the landing site is about 30 m and 35 m, respectively (Fig.3)[15]. The cumulative thickness of ejecta is consistent with the difference in elevation between the landing site and the basalts at the base of the Von Kármán crater[15]. The Finsen impact crater formed a large string of secondary craters on the lunar mare basalt at the base of both the Von Kármán and Leibniz impact craters, and the secondary craters are extremely well preserved on the lunar mare at the base of the Leibniz impact crater with well-defined crater rims, while the secondary craters of Finsen craters are highly degraded on the lunar mare at the base of the Von Kármán impact craters. Two profiles of ejecta, detected

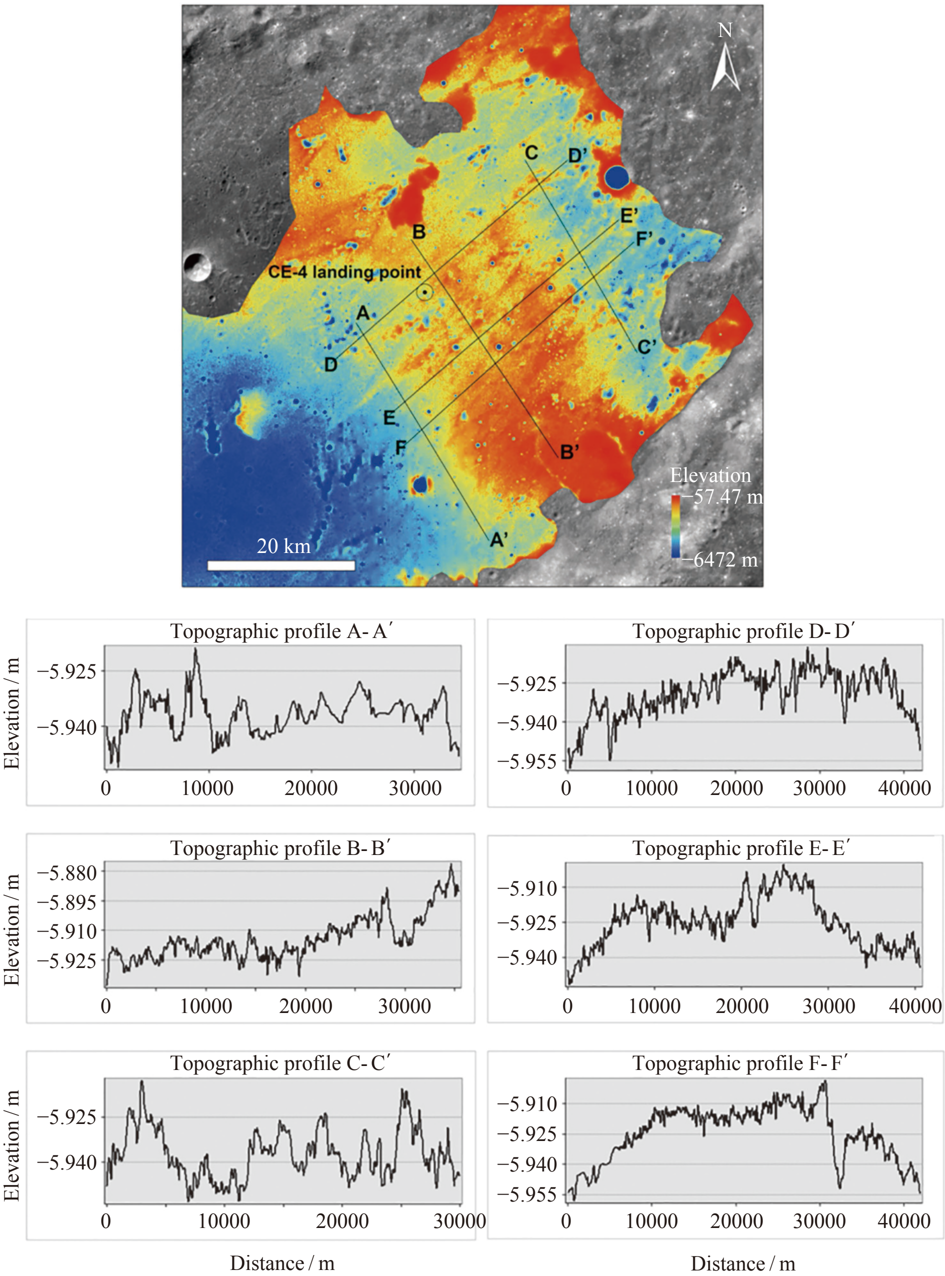

Fig. 3 SLDEM2015 and topographic profiles of the context of the Chang'E-4 landing site

by LPR, from a small fresh impact crater show that the ejecta is not the dense rocks excavated by the impact, but the loose lunar soil closed by instantaneous pore closure under the impact effect. The study suggests that the lunar mare basalts at the base of the Von Kármán impact crater may have been filled with large amounts of loose impact ejecta prior to the formation of the Finsen impact crater, resulting in a smaller initial topography and faster degradation rate in the subsequently superimposed Finsen secondary crater here, indicative of a more ancient subsurface source of material[16].

2.1.3 Characteristics of Lunar Soil and Gravel

Using the LPR high-frequency channel data and the three-dimensional velocity tracking method, the dielectric constant of the material in the depth below the lunar rover path down to 50 m was obtained and found to be similar to that of typical lunar soil material. The average value of the estimated dielectric constant from the lunar surface down to 4 cm is about 3.11 ± 0.085, and there are about 93 locations with dielectric constants larger than 4, indicating high-density non-lunar soil characteristics (Fig.4)[17]. The estimated loss angle tangent of the high-frequency LPR within about 400 ns is about 0.005, indicating that the dielectric properties of the material in the surface layer larger than 40 m are similar to those of typical lunar soil material. The overall rock abundance in the Chang’E-4 landing area is very low, about 0.21%, which is typical characteristics of mature lunar soil. In the vertical profile, the thickness of lunar soil on the roving route is about 12 m. The average particle size of lunar soil material increases with depth, indicating that the lunar soil production rate at the landing site may be much larger than the normal lunar soil production rate on the lunar surface. The high maturity of the lunar soil at the landing site revealed by the rover traces, reveals the relative influence of local topography and spatial weathering rate on the strength of the lunar soil. It is believed that the high dielectric constant region in the mature lunar soil is caused by surface exposure or buried rocks, and the distribution of lunar surface rock fragments provides new clues to decipher the formation and evolution of lunar soil[7, 16–22].

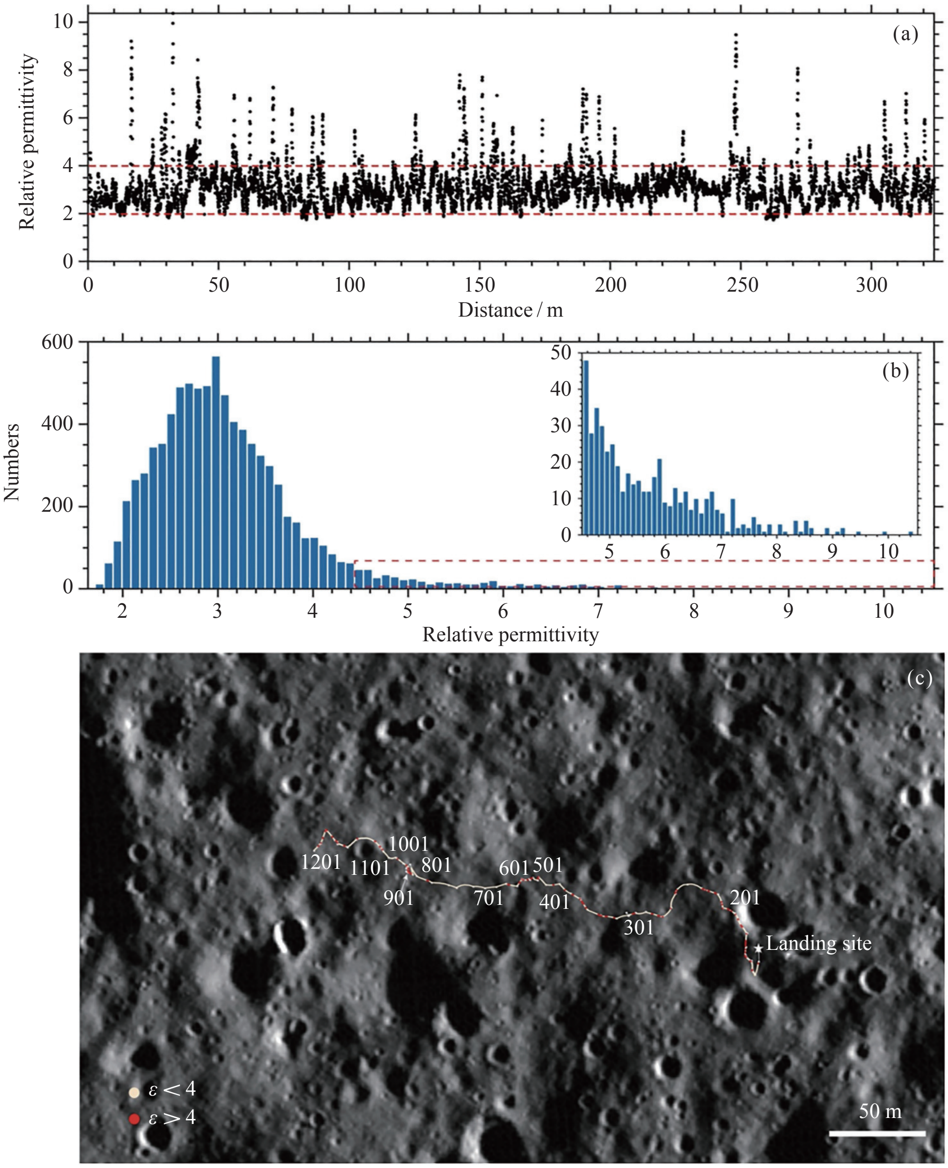

Fig. 4 Relative permittivity derived for the top-most (about 4 cm thick) regolith along the path of Yutu-2 in the first 12 lunar days

2.2 Deep Material and Material Composition of the Landing Region

2.2.1 Luminosity, Thermal Radiation Characteristics and Space Weathering of Lunar Soil in the Landing Region

An *in-situ* photometric experiment was conducted by using VNIS on the same region of the lunar surface during the tenth lunar day, and the spectra of the same target were successfully obtained under the conditions of different observational geometric angles of solar altitude and orientation (see Fig.5)[23]. It was found that the quality of the spectral data gradually decreases as the solar altitude angle decreases, which affects the accuracy of the inversion of the composition of the materials[23–26].

VNIS measured a series of spectra from the same region of the lunar surface and at different moments of the same lunar day to further confirm the lifting characteristics of the reflected spectra after 2 μm under high temperature conditions at the lunar surface, and the results show that the thermal contribution in the reflected spectra significantly increases the pyroxene and/or glass abundance at the landing site surface temperature of 346±8 K from 14:28 to 14:41 lunar local time (see Fig.6)[27]. The thermal contribution in the reflectance spectra significantly increases the estimation error of pyroxene and/or glass abundance, and the thermal radiative character is found to be significantly influenced by the microscale roughness in addition to the material composition[27].

Based on the maximum similarity between the simulated spectra and the in-situ measured spectra of Yutu-2, it is estimated that the sub-microscopic Fe content of the lunar soil in the Chang'E-4 landing region is about (0.32±0.06) wt.% and the FeO content is about (12.6±0.6) wt.%. The calculation shows that the maturity of the lunar soil in the landing region is 82±15, which indicates that the lunar soil in the Chang'E-4 landing region, mainly originating from the Finsen impact crater ejecta, is highly likely to be mature lunar soil[12]. It indicates that the rapid formation process of lunar soil in the Chang'E-4 landing region adequately mixed the most surficial of highly mature lunar soil, which is consistent with the geological background that the landing region has experienced more than 3 billion years of space weathering.

2.2.2 Characteristics of deep Material Composition and Distribution in the Landing Region

Von Kármán crater is predominantly flooded by low-Ti basalts (1.5 wt.%–3 wt.% TiO_2), rich in clinopyroxene and low in olivine. The basalts are affected by ejecta from the Finsen crater, with obvious compositional heterogeneity and lower FeO (content compared to the lunar mare basaltic samples). Local basalts not affected by the Finsen crater ejecta were excavated by the Zhinyu crater lying in the west of the landing site. The composition of the basalt varies with depth, suggesting Von Kármán crater has experienced at least three lava flooding events, and thus has formed three basaltic layers. The relatively homogeneous Mg values, *i.e.* Mg/(Fe+Mg), of the olivine among the three basaltic layers suggest that the source of the three mare basalts may have similar compositions or may be from a magma chamber where the melt composition evolved over time. The non-mare materials from craters such as Finsen have a different composition, with the central peaks characterized by an Mg-rich, low-Ca pyroxene composition, and the crater walls and their ejecta by relatively Fe/Ca-rich pyroxene compositions. These characteristics are consistent with the mineralogies of the pyroxene-bearing zone and compositional anomaly zone in the South Pole-Aitken Basin[9].

The analysis of infrared spectral data by spectral parameter analysis, spectral unmixing, and spectral matching indicates that the different exploration targets on the Yutu-2 rover roving route may have inhomogeneous material composition, and various rock types such as plagioclase, saprolite/gabbro have been identified, revealing the mixing degree of different source reservoirs from Von Kármán basalt, South Pole-Aitken impact melt, lunar mantle material, and crustal source ejecta material[28].

The interpretation results of the spectra of the first two detection points of the first lunar day, by using the modified Gaussian model, show that the detection target has the highest olivine content, followed by low-calcite pyroxene and the least high-calcite pyroxene. The relative content ratios of olivine, low-calcite pyroxene and high-calcite pyroxene minerals of the two detection points are 48:42:10 and 55:38:7, respectively[29]. The matching results of the spectral lookup table built based on the Hapke radiative transfer model found that the detection targets of the first two lunar days had a high con-

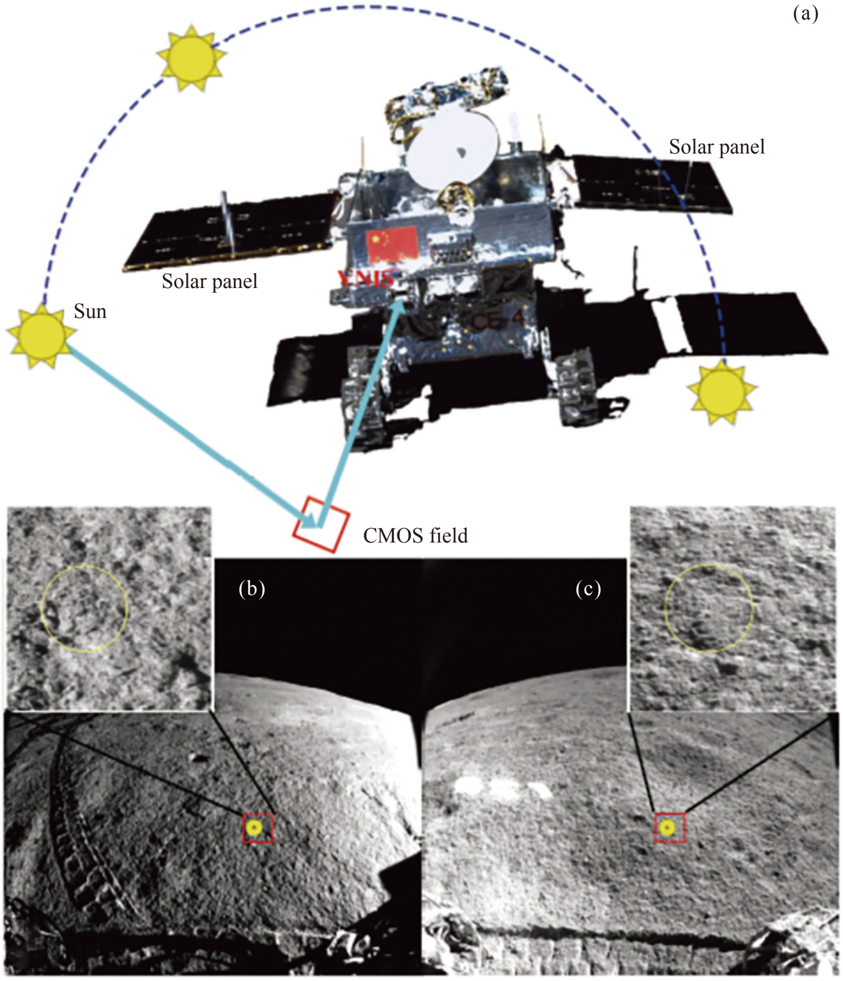

Fig. 5 Spectrophotometric measurements of lunar regolith by the Yutu-2 rover

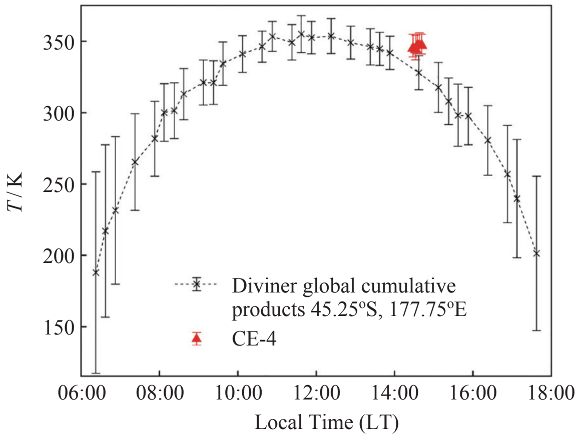

Fig. 6 Temperature at the Chang'E-4 landing site

tent of plagioclase, about 60%, and a low content of magnesian-irony minerals[30]. Empirical model calculations based on Apollo samples found that the lunar soil targets of the first three lunar days generally contain close to 60% of clastic agglomerates and fewer magnesian and iron minerals such as olivine, which is consistent with the landing region having undergone a longer period of space weathering[31]. The analysis based on the combination of spectral parameters such as absorption position and band area ratio reveals that the target spectra of the first three months of diurnal loam are dominated by olivine and pyroxene features, and the pyroxene minerals are dominated by monoclinic pyroxene with a composition between high and low calcium pyroxene, and this pyroxene composition is consistent with the rapid cooling crystallization of the magma[32].

The Yutu-2 lunar rover carried out the first spectroscopic detection of the rock target on the third lunar day, and the fitting results of the modified Gaussian model indicated that the magnesium-rich olivine and magnesium-rich plagioclase minerals in the rock were essentially equivalent[33, 34]. Analysis based on the Hapke radiative transfer model finds that the clasts contain about 48% plagioclase, about 38% low-calcium pyroxene, and about 14% olivine, corresponding to olivine-bearing thalassic rocks[31]. The clasts have a moderately fine-grained structure and are unlikely to be plutonic rocks, but are consistent with the rapid crystallization conditions of magma lakes formed by the South Pole-Aitken Basin impact[31]. The match results between the stone spectra and the spectra of lunar rocks and lunar meteorites in the NASA RELAB database indicate that the stone is enriched in plagioclase minerals (60%–80%), probably from the ejecta of the Zhinyu impact crater [35].

The combination of Hapke model and sparse unmixing algorithm was used to obtain the mineral content and chemical composition information of detection targets in the first 21 lunar days. The mineral composition is dominated by plagioclase, followed by pyroxene and little olivine, which corresponds to the mineralogical characteristics of norite/gabbro, and the content of low-calcium pyroxene exceeds that of high-calcium pyroxene in most of the detection targets. In terms of chemical composition, FeO content varies widely (7.42 wt.%–18.82 wt.%), TiO_2 content is generally low (1.48 wt.%–2.1 wt.%), while Mg values are low-medium ($Mg^{\#}$ about 55)[36, 37].

Synthesizing the results of existing in situ spectra of the Chang'E-4 landing and roving region, most studies suggest that the main mineral in the area is plagioclase, followed by pyroxene (more low-calcium pyroxene than high-calcium pyroxene), and less olivine. The material composition and rock structure characteristics suggest that the South Pole-Aitken Basin basement is likely not a single genesis of material such as primitive deep lunar material exposed by simple excavation or differentiated crystallization in impact melt lakes, but a mixture of multiple sources, indicating the complexity of the South Pole-Aitken Basin composition and geological processes.

2.2.3 Discovery of Impact Remnants and Impact Glass from Carbonaceous Chondrite

During the 8th and 9th lunar days of the mission's operation, the rover approached a small fresh impact crater and discovered some mysterious "glassy" materials around the center (Fig.7)[38]. The spectral analysis of this "glassy" material shows that it is similar to the Apollo impact melt breccias 70019 and 15546[39]. The detailed spectral analysis shows that the material contains a large amount of impact glass, which might be formed from another larger impact crater, suggesting that the lunar soil is evolving and maturing in the process of repeated impact smashing and welding into rock. This provides a new perspective to understand the formation mechanism of lunar soil[25]. The comparison with the spectra of a large number of carbonaceous chondrites shows that the "glassy" material has a high spectral similarity with the carbonaceous meteorite. The quantitative unmixing analysis using the radiative transfer model shows that the carbonaceous chondrite component in the "glassy" material is over 40 wt.%. The formation age of this small impact crater estimated based on impact crater degradation models suggest that the crater should have formed within one million years ago. Similar carbonaceous chondrite remnants may be common on the lunar surface[38].

Several centimeter-diameter translucent glass spheres were found on the moon. It is the first international discovery of hand specimen-sized, translucent, lunar glass spheres. Analysis revealed that the glass spheres are not the direct landing products of lunar volcanic activity or foreign impactors, but impact glass of special composition (Fig.8)[40], which may be a common material of lunar soil on the lunar highland. These findings have important implications for demonstrating that far impact glasses are inherent products of impact events on Earth-like objects, for inversion of the early impact history of the inner solar system, and for impact mechanics studies[40].

2.3 Subsurface Structure of Landing and Roving Region

The LPR high-frequency channel reveals structural information at depths larger than 40 m below the lunar surface of the roving route, divided into three main geological units (Fig.9)[20]. The first layer, about 0–12 m, is a layer of fine-grained lunar soil, with most of the material grain size less than 1 cm and fewer stones inside; the second layer, about 12–20 m, is a layer of ejecta mixed with fine-grained lunar soil and broken stones, in which a large number of stones are interspersed; the third layer, about 20–45 m, consists of discontinuous interlayer material with large differences in echo signals, showing alternating superposition of coarse-grained and fine-grained material. Studies by multiple teams have cross-

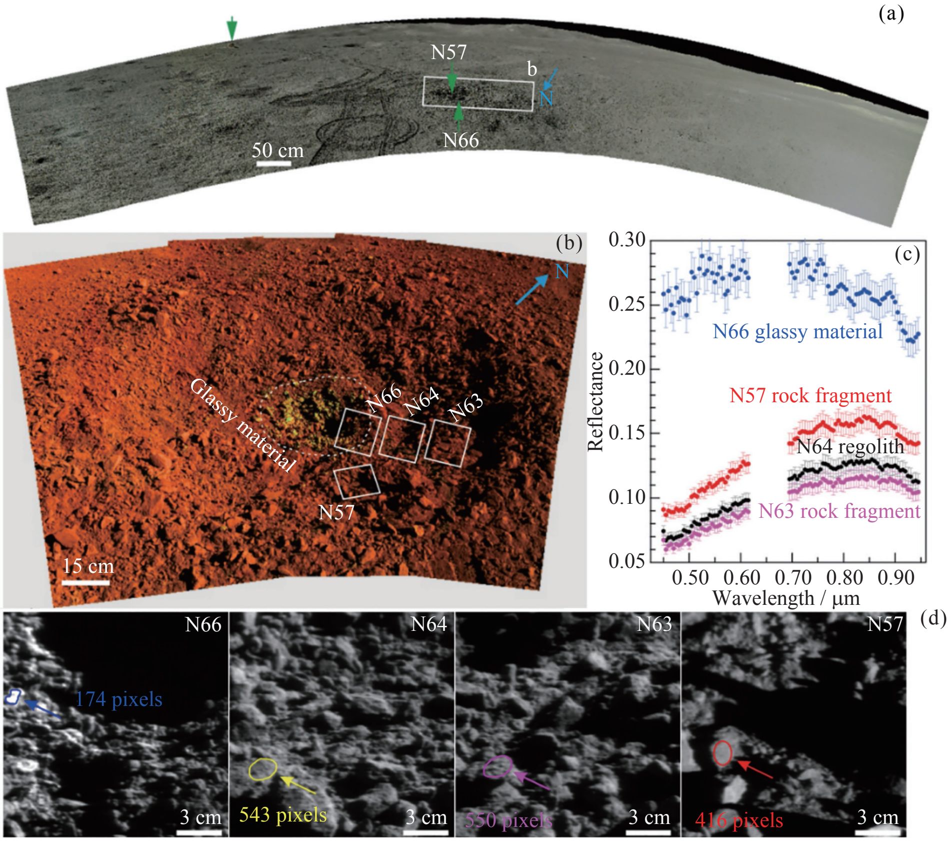

Fig. 7 Images and reflectance spectra of the targeted small crater

checked these three subsurface structures, but there are large differences in the upper and lower boundaries of each material layer and their source interpretations, reflecting the complex geological history of the younger lunar geological units[18, 20, 41–49].

The LPR low-frequency channel penetrates to a depth more than 400 m below the lunar surface, and the radar echo signal reveals at least three layers of deep (>40 m) subsurface structures (Fig.10)[46]. In terms of specific stratification and source interpretation, different interpretations have been obtained according to different data analysis methods and geological perspectives, and the main difference lies in the understanding of the source of the material within the surface layer to 100 m. Some views suggest that the material in this layer is mainly ejecta from different impact craters; other views suggest that the material at depth more than 40 m is mainly lunar mare basalt with some volcanic debris deposits interspersed by less late perturbations; some views also suggest that it is a spurious signal from LPR system itself[42, 46, 47, 50].

2.4 Lunar Surface Environment after Chang'E-4

2.4.1 Particle Radiation Environment on the Moon Surface

The analysis of the observational data obtained by LND during two lunar days from January to February 2019 shows that the particle radiation dose rate at the lunar surface is 13.2 μGy·h^{-1} (Si), of which the radiation dose rate of neutral particles (neutrons and gamma rays) is 3.1 μGy·h^{-1} (Si), accounting for about 23% of the total, with a quality factor of 4.32 and a dose equivalent of about 60 μSv·h^{-1} (Fig.11)[51]. There are significant differences between the cosmic ray energy spectra measured by LND, especially the proton energy spectrum, and the predictions given by the widely used CRÈME models: the mean values of the flux ratios between LND and the CRÈME96 and CRÈME2009 models reach 1.69 ± 0.17 and 2.25 ± 0.23, respectively, which provide strong constraints on the improvement of the CRÈME models, and the cosmic ray energy spectrum also provides tests and constraints for other related theoretical models. Observations data of LND over the 2-year period from Ja-

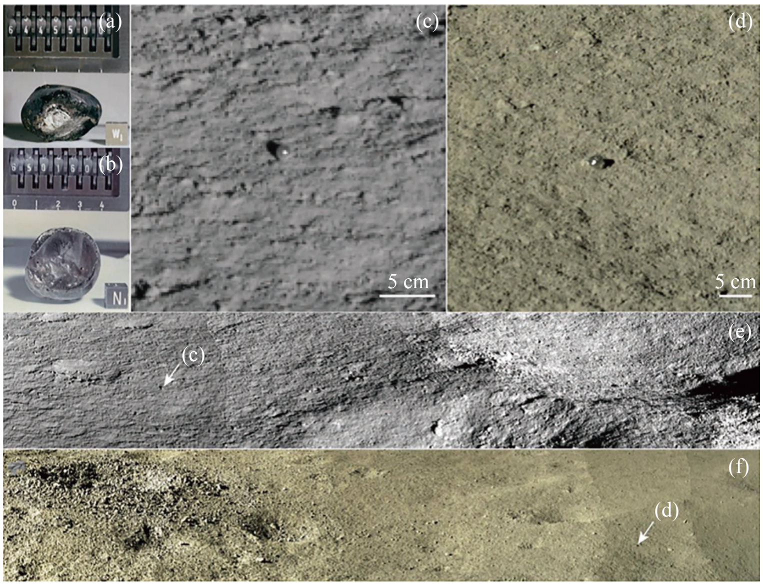

Fig. 8 Centimeter-sized glass globules collected by the Apollo 16 missions (a) (b) and those observed by the Chang'E-4 mission (c) (d). Note that the Apollo 16 mission was landed in the lunar highland, but the landing region was dominated by distal ejecta from the nearside. (e) (f) The two globules are accompanied by similar-sized fragments excavated by fresh impact craters nearby

nuary 2019 to December 2020 show that the average total absorbed dose rate of lunar surface particle radiation in silicon is 12.66 ± 0.45 μGy·h^{-1} and the absorbed dose rate of neutral particles is 2.67 ± 0.16 μGy·h^{-1}. The radiation dose rate shows a slow decrease with time over the 2-year period, while the change in the LET spectrum is small[51–54].

Observations by LND also confirm the morning and evening symmetry of the cosmic ray fluxes. Extraction of the ^{3}He/^{4}He flux ratio reveals a significant enhancement at about 12 MeV/nuclei and a very significant difference between the ^{3}He/^{4}He flux ratio values measured by LND and the predictions given by the GALPROP model, providing strong constraints on the GALPROP model as well as other related theoretical models[55].

On 6 May 2019, LND detected the first SEP event on the far side of the Moon. This event with a very small peak flux and short duration, is a typical impulsive solar energetic particle event (impulsive SEPs). Both electrons and protons were found to exhibit a good velocity dispersion distribution, showing that the time of particle release from the acceleration region is one hour earlier for electrons than for protons (Fig.12)[56]. Further analysis reveals that the energy inflection point is about 2.5 MeV and originates from an M1.0 class flare[56].

2.4.2 Interaction of the Solar Wind with the Moon

The observation results of ASAN show that the hydrogen ENA energy spectrum is in good agreement with the large-scale observations of Chandrayaan-1 and IBEX when the energy is higher than the solar wind ion energy above 0.1 $E_{\rm sw}$, while the hydrogen ENA fluxes measured by ASAN are higher than the results of Chandrayaan-1 and IBEX when the energy is lower than 0.1 $E_{\rm sw}$[57]. The component above 0.1 $E_{\rm sw}$ is mainly hydrogen ENA generated by the backscattering of solar wind ions, and the component below this energy is mainly ENA from the sputtering of lunar surface material[57, 58].

Analysis of the ENA energy spectrum from January 2019 to October 2020 reveals that the ENA differential fluxes on the dawnside are higher than those on the dusk side during most lunar days, and the ENA differential fluxes in different energy ranges on the dawnside and duskside are positively correlated with solar wind state parameters such as flux, density, and dynamic pressure. The cutoff energy and temperature of ENA on the duskside are lower than those on the dawnside under the same energy solar wind bombardment[59], suggesting that the solar wind on the duskside may be af-

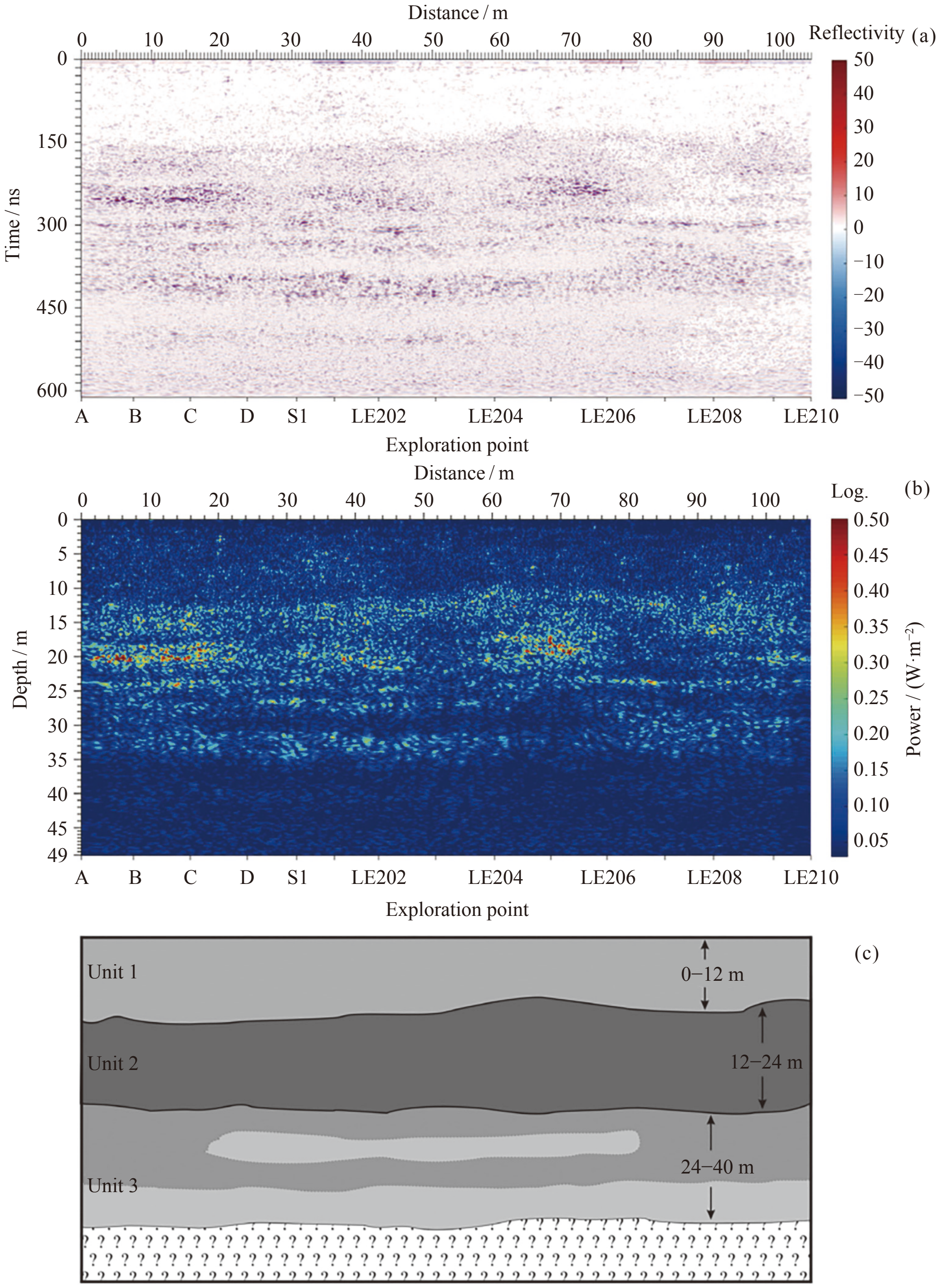

Fig. 9 LPR data at 500 MHz. (a) LPR 500-MHz radargram represented in standard seismic colors after applying Dewow, background subtraction, and Spherical and Exponential Compensation (SEC) gain and migration. (b) Tomographic reconstruction of the radar data, where red represents high reflectivity and blue is low reflectivity. (c) Schematic of the stratigraphic sequence highlighting the contacts between units and the relevant thicknesses based on the radargram and the tomographic reconstruction

fected by the lunar micro-magnetosphere and slowed down by the electrostatic field above the magnetic anomaly, resulting in a narrower energy spectrum and lower temperature[59].

2.4.3 First Observation of the Lunar Mini-magnetosphere on the Lunar Surface

The landing site of Chang’E-4 is located at the eastern edge of the mare imbrium antipodal region, the largest

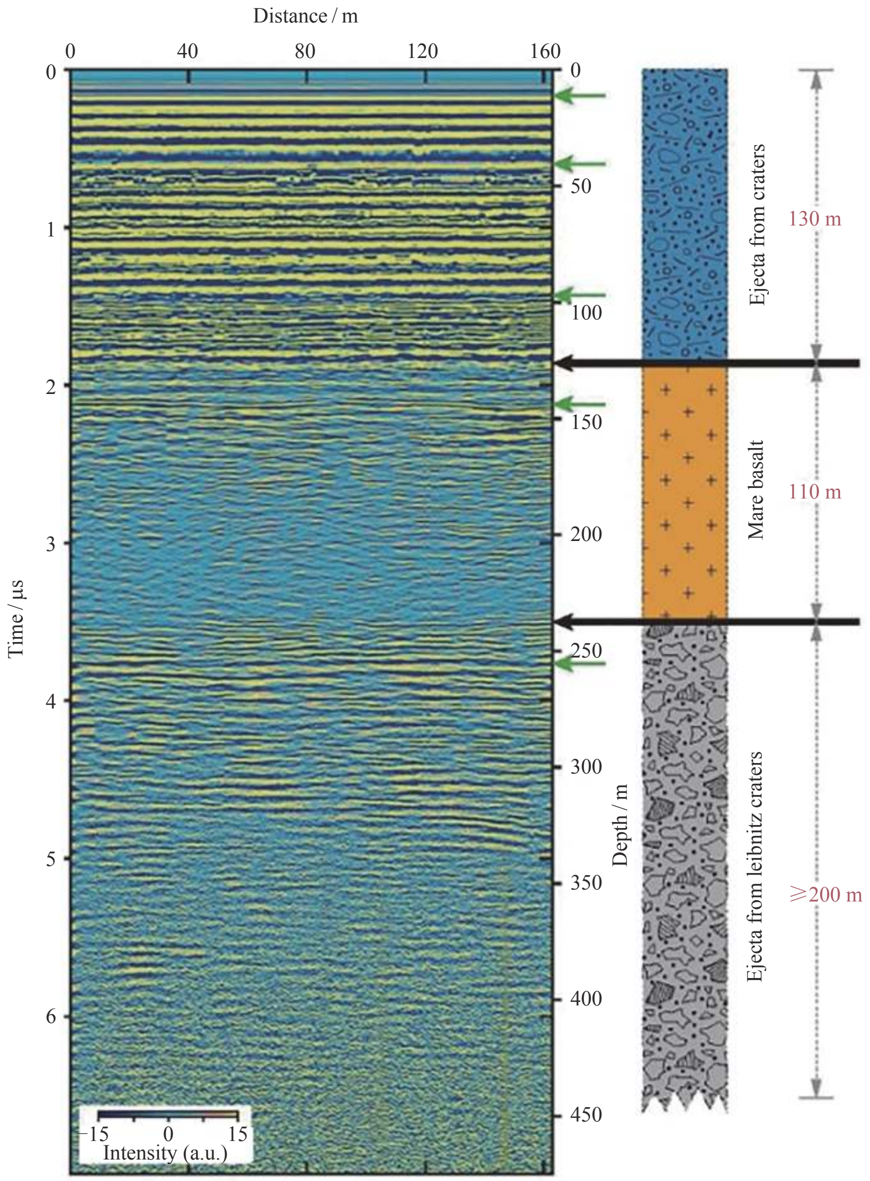

Fig. 10 Low-frequency LPR profile along the track of the Yutu-2 rover

magnetic anomaly of the Moon. When Chang'E-4 is downstream of the magnetic anomaly (duskside), the overall particle flux measured by the neutral atom detector is lower than that measured when it is upstream of the magnetic anomaly (dawnside)[60]. Combined with global Hall MHD simulations, it is confirmed that the lunar mini-magnetosphere is responsible for the flux difference, and the effect of the micro-magnetosphere on the solar wind is mainly deflection and deceleration, rather than complete blockage of the solar wind, with an average blockage efficiency of about 50%[60].

2.5 Lunar Low-frequency Radio Observations

The relay communication satellite and the lander of Chang'E-4 mission separately carry two science payloads, NCLE and LFS. Their objectives are exploring the electromagnetic wave radiation environment on the far side of the Moon and in lunar space, detecting solar HF-VHF band bursts during peak solar activity years.

Since the lander of Chang'E-4 is the backup model of the Chang'E-3 lander, the electromagnetic shielding design specifically for low-frequency radio observation cannot be carried out, and the noise from the probe platform brings serious impact on low-frequency radio observation (Fig.13)[61]. When designing the instrument, a short antenna was added and a pair-cancellation algorithm was used to reduce the detector background noise,

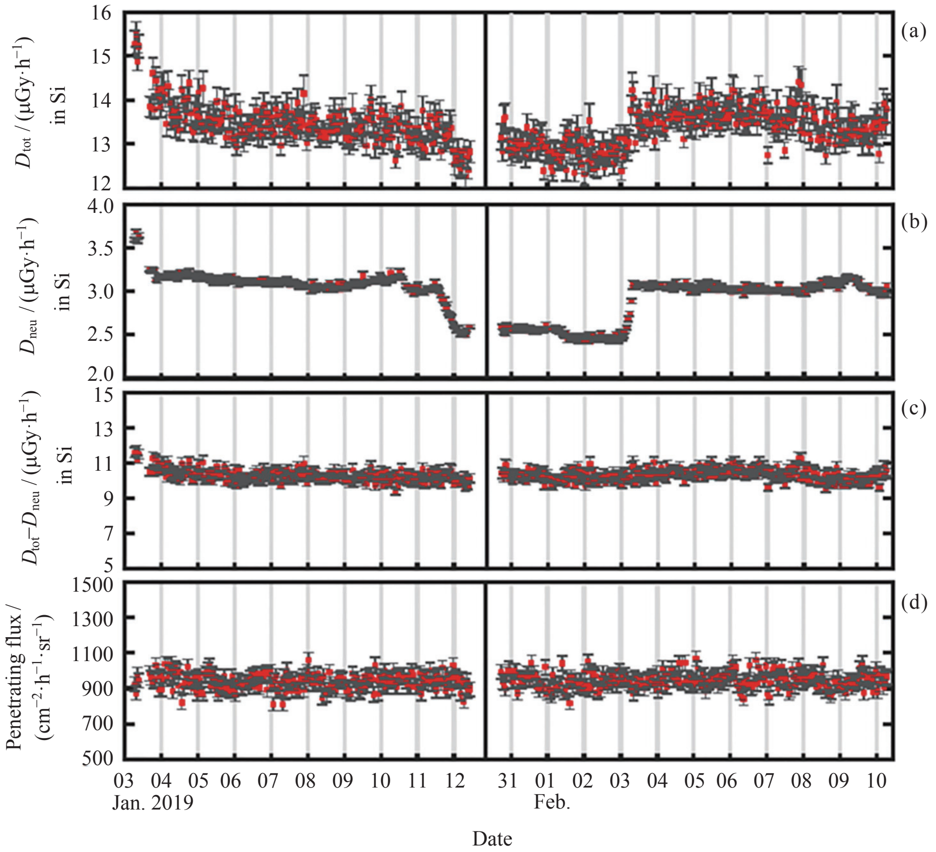

Fig. 11 Temporal evolution of the radiation environment on the Moon as measured by LND on Chang’E-4 during the first and second lunar days after Chang’E-4 landed

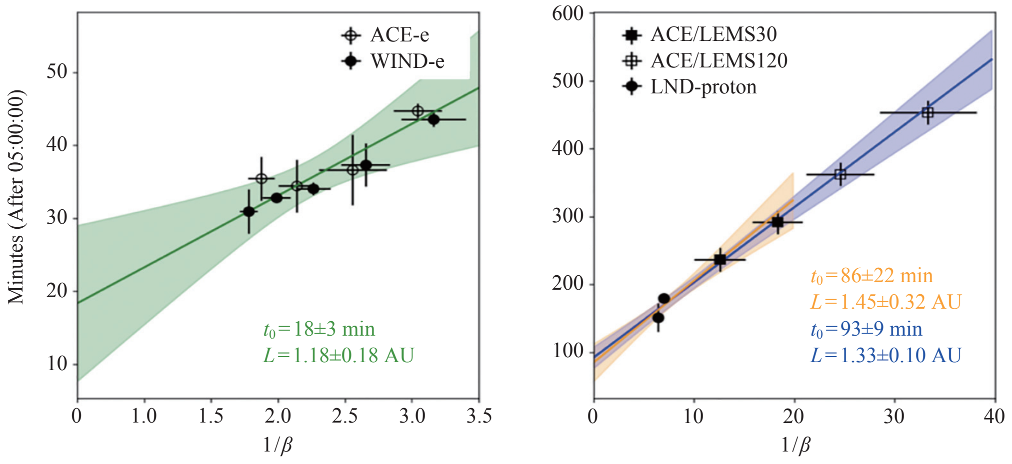

Fig. 12 Velocity dispersion analysis of the SEPs on 6 May 2019 (electrons shown in the left and protons shown in the right panel). Wind and ACE electron data are used to determine the electron release time

however this could not be completely eliminated[61]. Therefore, a thematic assessment of the achievability of the scientific goal of low-frequency radio detection was conducted, and concluded that when the solar flux density is less than 10^{-21} W·m^{-2}·Hz^{-1}, the low-frequency radio spectrometer cannot detect the solar low-frequency radio radiation; When the flux density of the solar burst is greater than 10^{-18} W·m^{-2}·Hz^{-1}, the solar low-frequency radio radiation can be detected in 100 kHz to 8 MHz; When the peak flux density of the solar burst is greater

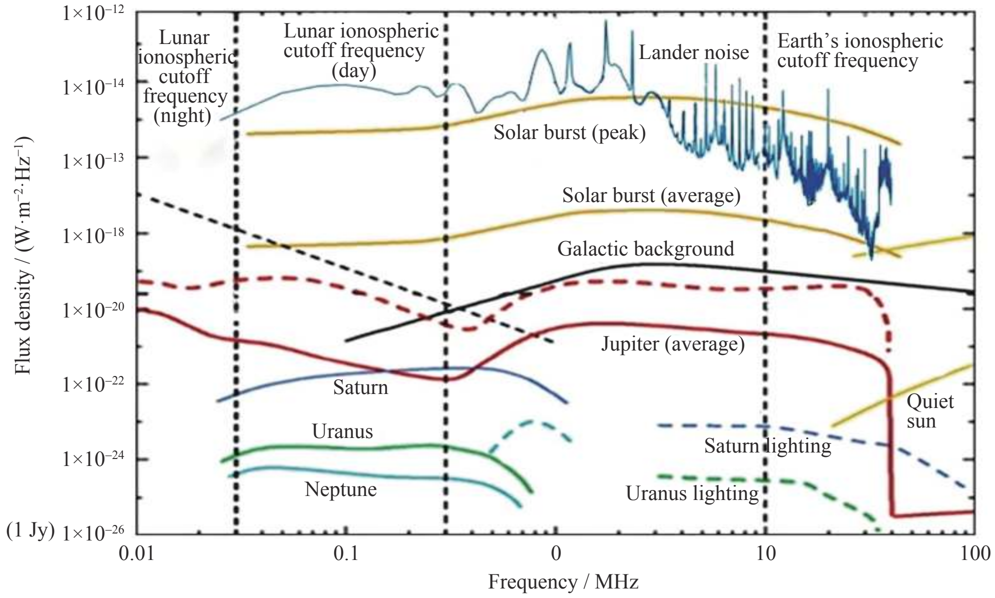

Fig. 13 Radio emission levels on surface of the Moon

than 10^{-16} W·m^{-2}·Hz^{-1}, the solar low-frequency radio radiation can be detected in the full frequency band from 100 kHz to 40 MHz.

LFS has worked 41 lunar days for scientific observations. Tests confirm the noise deduction effect is basically consistent with the ground test. A three-antenna spectrum is generated by using detection data, so it is known that LFS can obtain radio phenomena similar to the solar burst, and data processing methods for cosmic background radiation and other stable spectral signal are also effective[62]. Unfortunately, no significant scientific phenomena have been found so far.

3 Future Prospects

At present, the lander and rover of Chang'E-4 have been working normally on the far side of the Moon for more than 3 years. All systems are working normally. Yutu-2 lunar rover is walking to the northwest direction, and plans to detect the lunar mare basalt area with thin ejecta coverage. Currently, the rover has travelled about 1.1 km. The Chang'E-4 mission has demonstrated the high richness and complexity of lunar geological processes over a longer roving route. Although the current scientific understanding is still controversial for the interpretation of some phenomena, it is still expected to further reveal the evolution of the surface topography and geological structure of the landing region in three dimensions, providing a basis for comparison to correct and constrain the existing geological interpretation. 2021–2024 are solar maximum years, and the LFS/NCLE is expected to have the opportunity to obtain solar burst detection results.

In 2021, Phase IV of China's lunar exploration project was kicked-off. Taking advantage of a long period of continuous solar illumination at the lunar south pole, different detection means such as orbiting and remote sensing, landing and in-situ detection, roving, leaping and sampling can be used on the following subjects: (i) detection of volatiles in the lunar south pole and distribution and storage of water in lunar soil in permanent shadow area; (ii) assessment of fugacity, content, distribution and origin of lunar water; (iii) *in-situ* utilization experiments of lunar rare gas and other resources; (iv) in-depth exploration of the lunar space environment, deep material, internal structure; (v) obserbvation on earth and astronomical objects from the moon as a platform; (vi) experiments in the micro-enclosed terrestrial ecosystems under the lunar surface environment. Basic model of the lunar research station will be established to carry out large-scale, full-scale, long-period scientific observations and researches, to gain scientific understanding.

Acknowledgments High tribute should be paid to the core scientific research team of the Chang'E-4 mission for providing information and assistance. Thanks to LIU Yang, GOU Sheng, LIN Honglei, XIAO Zhiyong, ZHANG Jinhai, HUANG Jun, LI Lei, CAO Jinbin for providing material and suggestions to the manuscript.

References

[1] LIU J J, REN X, YAN W, *et al.* Descent trajectory reconstruction and landing site positioning of Chang'E-4 on the lunar farside[J]. *Nature Communications*, 2019, **10**(1): 4299

[2] CLEP: Yutu-2 lunar rover travels more than 1,000 meters, [EB/OL]. 2022 [2022]. https://mp.weixin.qq.com/s/utRYQ7WbGiQNql1engYJmQ

[3] CHEN Yuesong, HAN Juanjuan, FAN Yu, ZOU Yongliao, WANG Chi. Overview of the Latest Scientific Results of China's Lunar Exploration Program. Chin. J. Space Sci. , 2020, 40(5): 626-642

[4] WANG Chi, XU Lin, ZOU Yongliao. The latest scientific results from Chang'E-4 mission (in Chinese). 2020 Scinece Development Report[M]. Beijing: Science Press, 2021, 29-39

[5] WANG C, LI L, ZHANG A B, *et al.* The solar wind and particle radiation environment on the surface of the Moon-new observations from Chang'E-4[J]. *Journal of Deep Space Exploration*, 2022, **9**(3): 239-249

[6] JIA Y Z, ZOU Y L, PING J S, *et al.* The scientific objectives and payloads of Chang'E-4 mission[J]. *Planetary and Space Science*, 2018, **162**: 207-215

[7] WU B, LI Y, LIU W C, *et al.* Centimeter-resolution topographic modeling and fine-scale analysis of craters and rocks at the Chang'E-4 landing site[J]. *Earth and Planetary Science Letters*, 2021, **553**: 116666

[8] FU X H, QIAO L, ZHANG J, *et al.* The subsurface structure and stratigraphy of the Chang'E-4 landing site: orbital evidence from small craters on the Von Kármán crater floor[J]. *Research in Astronomy and Astrophysics*, 2020, **20**(1): 008

[9] GOU S, YUE Z Y, DI K C, *et al.* Mare basalt flooding events surrounding Chang'E-4 landing site as revealed by Zhinyu crater ejecta[J]. *Icarus*, 2021, **360**: 114370

[10] QIAO L, LING Z C, FU X H, *et al.* Geological characterization of the Chang'E-4 landing area on the lunar farside[J]. *Icarus*, 2019, **333**: 37-51

[11] JIA M N, DI K C, YUE Z Y, *et al.* Multi-scale morphologic investigation of craters in the Chang'E-4 landing area[J]. *Icarus*, 2021, **355**: 114164

[12] GOU S, YUE Z Y, DI K C, *et al.* In situ spectral measurements of space weathering by Chang'E-4 rover[J]. *Earth and Planetary Science Letters*, 2020, **535**: 116117

[13] GUO D J, FA W Z, ZENG X J, *et al.* Geochemistry of the Von Kármán crater floor and thickness of the non-mare ejecta over the Chang'E-4 landing area[J]. *Icarus*, 2021, **359**: 114327

[14] DING C Y, XIAO Z Y, WU B, *et al.* Fragments delivered by secondary craters at the Chang'E-4 landing site[J]. *Geophysical Research Letters*, 2020, **47**(7): e2020GL087361

[15] DI K C, ZHU M H, YUE Z Y, *et al.* Topographic evolution of Von Ka̍rma̍n crater revealed by the lunar rover Yutu-2[J]. *Geophysical Research Letters*, 2019, **46**(22): 12764-12770

[16] XIAO Z Y, DING C Y, XIE M G, *et al.* Ejecta from the Orientale basin at the Chang'E-4 landing site[J]. *Geophysical Research Letters*, 2021, **48**(3): e2020GL090935

[17] DING C Y, XIAO Z Y, WU B, *et al.* Rock fragments in shallow lunar regolith: Constraints by the lunar penetrating radar onboard the Chang'E-4 mission[J]. *Journal of Geophysical Research: Planets*, 2021, **126**(9): e2021JE006917

[18] LAI J L, XU Y, ZHANG X P, *et al.* Comparison of dielectric properties and structure of lunar regolith at Chang'E-3 and Chang'E-4 landing sites revealed by ground-penetrating radar [J]. *Geophysical Research Letters*, 2019, **46**(22): 12783-12793

[19] LAI J L, CUI F F, XU Y, *et al.* Dielectric properties of lunar materials at the Chang'E-4 landing site[J]. *Remote Sensing*, 2021, **13**(20): 4056

[20] LI C L, SU Y, PETTINELLI E, *et al.* The Moon's farside shallow subsurface structure unveiled by Chang'E-4 Lunar Penetrating Radar[J]. *Science Advances*, 2020, **6**(9): eaay6898

[21] SONG H J, LI C, ZHANG J H, *et al.* Rock location and property analysis of lunar regolith at Chang'E-4 landing site based on local correlation and semblance analysis[J]. *Remote Sensing*, 2021, **13**(1): 48

[22] TANG Z C, LIU J J, WANG X, *et al.* Physical and mechanical characteristics of lunar soil at the Chang'E-4 landing site[J]. *Geophysical Research Letters*, 2020, **47**(22): e2020GL089499

[23] LIN H L, YANG Y Z, LIN Y T, *et al.* Photometric properties of lunar regolith revealed by the Yutu-2 rover[J]. *Astronomy & Astrophysics*, 2020, **638**: A35

[24] LIN H L, XU R, YANG W, *et al.* In situ photometric experiment of lunar regolith with visible and near-infrared imaging spectrometer on board the Yutu-2 lunar rover[J]. *Journal of Geophysical Research: Planets*, 2020, **125**(2): e2019JE006076

[25] LIN H L, LIN Y T, YANG W, *et al.* New insight into lunar regolith-forming processes by the lunar rover Yutu-2[J]. *Geophysical Research Letters*, 2020, **47**(14): e2020GL087949

[26] YANG Y Z, LIN H L, LIU Y, *et al.* The effects of viewing geometry on the spectral analysis of lunar regolith as inferred by *in situ* spectrophotometric measurements of Chang'E-4[J]. *Geophysical Research Letters*, 2020, **47**(8): e2020GL087080

[27] LIN H L, LI S, LIN Y T, *et al.* Thermal modeling of the lunar regolith at the Chang'E-4 landing site[J]. *Geophysical Research Letters*, 2021, **48**(6): e2020GL091687

[28] HUANG J, XIAO Z Y, XIAO L, *et al.* Diverse rock types detected in the lunar South Pole–Aitken Basin by the Chang'E-4 lunar mission[J]. *Geology*, 2020, **48**(7): 723-727

[29] LI C L, LIU D W, LIU B, *et al.* Chang'E-4 initial spectroscopic identification of lunar far-side mantle-derived materials [J]. *Nature*, 2019, **569**(7756): 378-382

[30] HU X Y, MA P, YANG Y Z, *et al.* Mineral abundances inferred from in situ reflectance measurements of Chang'E-4 landing site in South Pole-Aitken basin[J]. *Geophysical Research Letters*, 2019, **46**(16): 9439-9447

[31] LIN H L, HE Z P, YANG W, *et al.* Olivine-norite rock detected by the lunar rover Yutu-2 likely crystallized from the SPA-impact melt pool[J]. *National Science Review*, 2020, **7**(5): 913-920

[32] CHEN J, LING Z C, QIAO L, *et al.* Mineralogy of Chang'E-4 landing site: preliminary results of visible and near-infrared imaging spectrometer[J]. *Science China Information Sciences*, 2020, **63**(4): 140903

[33] GOU S, DI K C, YUE Z Y, *et al.* Lunar deep materials observed by Chang'E-4 rover[J]. *Earth and Planetary Science Letters*, 2019, **528**: 115829

[34] GOU S, DI K C, YUE Z Y, *et al.* Forsteritic olivine and magnesium-rich orthopyroxene materials measured by Chang'E-4 rover[J]. *Icarus*, 2020, **345**: 113776

[35] MA P, SUN Y X, ZHU M H, *et al.* A plagioclase-rich rock measured by Yutu-2 Rover in Von Kármán crater on the far side of the Moon[J]. *Icarus*, 2020, **350**: 113901

[36] ZENG Q H, CHEN S B, ZHANG Y Z, *et al.* Mineralogical and chemical properties inversed from 21-lunar-day VNIS observations taken during the Chang'E-4 mission[J]. *Scientific Reports*, 2021, **11**(1): 15435

[37] Ling Z C, Qiao L, Liu C Q, *et al.* Composition, mineralogy and chronology of mare basalts and non-mare materials in Von Kármán crater: landing site of the Chang'E-4 mission[J]. *Planetary and Space Science*, 2019, **179**: 104741

[38] YANG Y Z, LI S, ZHU M H, *et al.* Impact remnants rich in carbonaceous chondrites detected on the Moon by the Chang'E-4 rover[J]. *Nature Astronomy*, 2022, **6**(2): 207-213

[39] GOU S, YUE Z Y, DI K C, *et al.* Impact melt breccia and surrounding regolith measured by Chang'E-4 rover[J]. *Earth and Planetary Science Letters*, 2020, **544**: 116378

[40] XIAO Z Y, YAN P, WU B, *et al.* Translucent glass globules on the Moon[J]. *Science Bulletin*, 2022, **67**(4): 355-358

[41] DONG Z H, FANG G Y, ZHAO D, *et al.* Dielectric properties of lunar subsurface materials[J]. *Geophysical Research Letters*, 2020, **47**(22): e2020GL089264

[42] LAI J L, XU Y, BUGIOLACCHI R, *et al.* First look by the Yutu-2 rover at the deep subsurface structure at the lunar farside[J]. *Nature Communications*, 2020, **11**(1): 3426

[43] LAI J L, XU Y, BUGIOLACCHI R, *et al.* A complex paleo-surface revealed by the Yutu-2 rover at the lunar farside[J]. *Geophysical Research Letters*, 2021, **48**(20): e2021GL095133

[44] GIANNAKIS I, ZHOU F, WARREN C, *et al.* Inferring the shallow layered structure at the Chang'E-4 landing site: a novel interpretation approach using lunar penetrating radar[J]. *Geophysical Research Letters*, 2021, **48**(16): e2021GL092866

[45] XU L Y, ZHANG X Y, QIAO L, *et al.* Evaluating the thickness and stratigraphy of ejecta materials at the Chang'E-4 landing site[J]. *The Astronomical Journal*, 2021, **162**(1): 29

[46] ZHANG J H, ZHOU B, LIN Y T, *et al.* Lunar regolith and substructure at Chang'E-4 landing site in South Pole –Aitken basin[J]. *Nature Astronomy*, 2021, **5**(1): 25-30

[47] ZHANG L, LI J, ZENG Z F, *et al.* Stratigraphy of the Von Kármán crater based on Chang'E-4 lunar penetrating radar data[J]. *Geophysical Research Letters*, 2020, **47**(15): e2020 GL088680

[48] ZHANG L, XU Y, BUGIOLACCHI R, *et al.* Rock abundance and evolution of the shallow stratum on Chang'E-4 landing site unveiled by lunar penetrating radar data[J]. *Earth and Planetary Science Letters*, 2021, **564**: 116912

[49] ZHOU H Q, FENG X, DONG Z J, *et al.* Application of denoising CNN for noise suppression and weak signal extraction of lunar penetrating radar data[J]. *Remote Sensing*, 2021, **13**(4): 779

[50] YUAN Y F, ZHU P M, XIAO L, *et al.* Intermittent volcanic activity detected in the Von Kármán crater on the farside of the Moon[J]. *Earth and Planetary Science Letters*, 2021, **569**: 117062

[51] ZHANG S Y, WIMMER-SCHWEINGRUBER R F, YU J, *et al.* First measurements of the radiation dose on the lunar surface[J]. *Science Advances*, 2020, **6**(39): eaaz1334

[52] HOU D, ZHANG S, YU J, *et al.* Removing the dose background from radioactive sources from active dose rate measurements in the Lunar Lander Neutron & Dosimetry (LND) experiment on Chang'E 4[J]. *Journal of Instrumentation*, 2020, **15**: P01032

[53] WIMMER-SCHWEINGRUBER R F, YU J, BÖTTCHER I, *et al.* The lunar lander neutron and dosimetry (LND) experiment on Chang'E 4[J]. *Space Science Reviews*, 2020, **216**(6): 104

[54] ZHANG S Y, HOU D H, WIMMER-SCHWEINGRUBER R F, *et al.* Radiation dose of LND on the lunar surface in two years[J]. *Chinese Journal of Space Science*, 2021, **41**(3): 439-444

[55] LUO P W, ZHANG X P, FU S, *et al.* First measurements of low-energy cosmic rays on the surface of the lunar farside from Chang'E-4 mission[J]. *Science Advances*, 2022, **8**(2): eabk1760

[56] XU Z G, GUO J N, WIMMER-SCHWEINGRUBER R F, *et al.* First solar energetic particles measured on the lunar farside[J]. *The Astrophysical Journal Letters*, 2020, **902**(2): L30

[57] ZHANG A B, WIESER M, WANG C, *et al.* Emission of energetic neutral atoms measured on the lunar surface by Chang'E-4[J]. *Planetary and Space Science*, 2020, **189**: 104970

[58] WIESER M, BARABASH S, WANG X D, *et al.* The advanced small analyzer for neutrals (ASAN) on the Chang'E-4 rover yutu-2[J]. *Space Science Reviews*, 2020, **216**(4): 73

[59] WANG H Z, XIAO C, SHI Q Q, *et al.* Energetic neutral atom distribution on the lunar surface and its relationship with solar wind conditions[J]. *The Astrophysical Journal Letters*, 2021, **922**(2): L41

[60] XIE L H, LI L, ZHANG A B, *et al.* Inside a lunar mini-magnetosphere: first energetic neutral atom measurements on the lunar surface[J]. *Geophysical Research Letters*, 2021, **48**(14): e2021GL093943

[61] ZHANG Tao, SU Yan. Research of the method for reducing background of very low frequency radio spectrumon Chang'E-4[J]. *Astronomical Research & Technology*, 2019, **16**(3): 312-320

[62] JIAO Kang, WANG Mingyuan, ZHANG Tongjie, *et al.* Analysis of the capability of Chang'E-4 low frequency radio spectrometer 2 C data in detecting the dark ages[J]. *Astronomical Research & Technology*, 2021, **18**(4): 472-476